Noise-induced limits of detection in frequency locked optical microcavities

Shuang Hao and Judith Su

Abstract—Ultra-high quality (Q) whispering gallery mode (WGM) optical microcavities have been shown to be sensitive biomolecular sensors due to their long photon confinement times. We have previously experimentally demonstrated that a system known as FLOWER (frequency locked optical whispering evanescent resonator) can detect single macromolecules. FLOWER uses frequency locking in combination with balanced detection and data processing to greatly improve the sensitivity, stabilization, signal-to-noise ratio (SNR), and the detection limit of ultra-high-Q microcavities. Here we present the analytical basis for FLOWER and explore its limits of detection via numerical simulation. We examine the effects of key parameters such as Qfactor and frequency modulation depth on the SNR of FLOWER. We demonstrate that the frequency locked optical microcavity system is limited by the shot noise from the receiver, as well as the laser intensity noise. Using median filtering in combination with step-fitting algorithms, frequency locked ultra-high-O microcavities can detect resonance shifts as small as 0.05 attometers at one millisecond time intervals. Our results can guide the choice of experimental parameters to achieve better sensing performance in a variety of target applications, including fundamental studies of protein-protein interactions and medical diagnostics and prognostics.

Index Terms—Frequency locked loops, microcavity resonators, noise cancellation, biosensing.

I. INTRODUCTION

In recent years, there has been a growing need for label-free ultra-sensitive biochemical sensors for early disease diagnostics and prognostics, environmental monitoring¹, public health monitoring of bacteria and viruses², and other applications. Imaging based techniques are mature technologies for detecting biological analytes, but these methods usually require labeling of particles with tags, which can be complex, time-consuming, labor-intensive, and costly.

We have previously developed a system known as FLOWER (frequency locked optical whispering evanescent resonator), which can detect single macromolecules in real time³. FLOWER works by actively tracking the shift in resonance wavelength caused by particles binding to an optical

We acknowledge partial financial support from the NIH R03AG055020, R21CA212712, NSF 1842045, Defense Threat Reduction Agency (DTRA) HDTRA1-18-1-0044, Gordon & Betty Moore Foundation (Grant GBMF7555.14), Flinn Foundation (Grant 26223) Arizona Alzheimer's Consortium, and the University of Arizona Cancer Center. S.H. is supported by the Jack D. Gaskill Graduate Student Scholarship in Optical Science.

S. Hao is with the Wyant College of Optical Sciences, University of Arizona, Tucson, AZ 85721, USA.

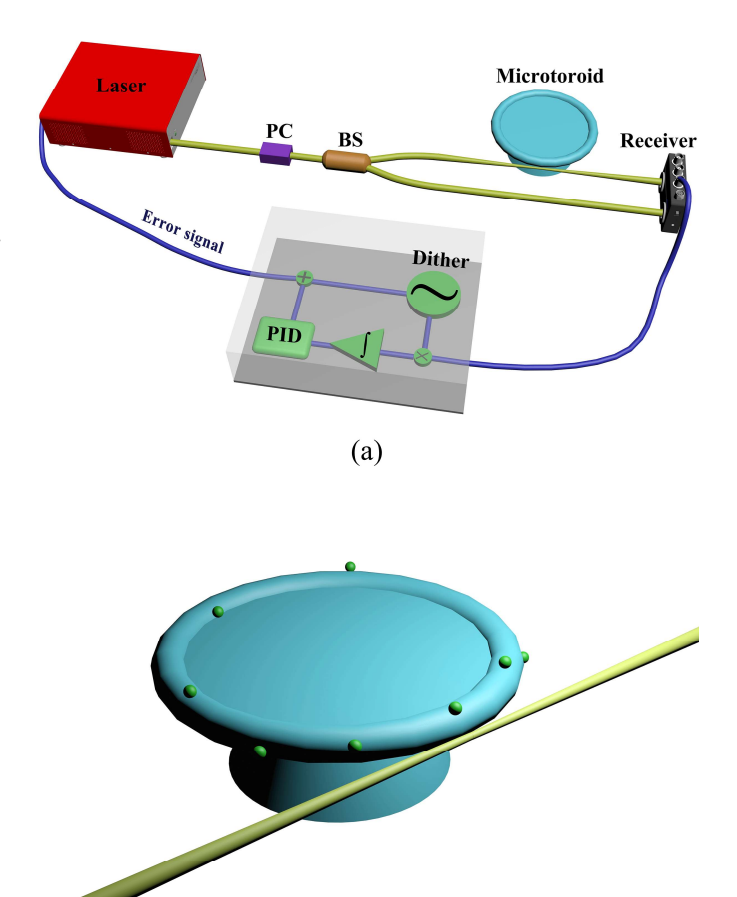


Fig. 1. Frequency Locked Optical Whispering Resonator (FLOWER) system. (a) A schematic diagram of the FLOWER system. A 2 kHz oscillation dither signal is used to modulate the laser frequency. A polarization controller (PC) is used to control the polarization of the laser. A 50:50 beam splitter (BS) splits the light into the signal and reference arms of an auto-balanced photoreceiver. The output from the auto-balanced receiver is multiplied by the dither signal and time averaged, thus generating an error signal, which is proportional to the frequency difference between the laser and the microcavity resonance. A proportional-integral-derivative (PID) controller sets the laser frequency to the microcavity resonance according to the received error signal. (b) Artistic rendering of a microtoroid optical resonator coupled to a tapered optical fiber in the presence of binding analyte particles.

(b)

J. Su is with the Wyant College of Optical Sciences and Department of Biomedical Engineering, University of Arizona, Tucson, AZ 85721, USA (e-mail: judy@optics.arizona.edu

microcavity. Ultra-high Q-factor microcavities⁴ such as microspheres⁵ and microtoroids⁶ offer two main advantages for biochemical sensing: on the one hand, they have narrow linewidth resonance, which contributes to measuring extremely small resonance shifts (on the order of attometers)⁷; on the other hand, their small mode volume enhances light-matter interaction, which provides the increased sensitivity needed for single particle detection⁸. Bioanalytes, such as viruses⁹, DNA oligomers¹⁰, bacteria¹¹, and proteins⁷, are challenging to detect in aqueous solutions as their refractive index is close to water.

Light continuously circulates in the resonator multiple times based on the principle of total internal reflection⁶. When particles adsorb or bind to the surface of a microcavity, they become polarized and cause the resonance frequency of the cavity to shift. The magnitude of this shift can be used for detecting and sizing particles. The resonance frequency shift may be calculated according to the Bethe-Schwinger cavity perturbation formula¹³. The relative frequency shift $\Delta\omega/\omega_0$ is the negative of the energy required to polarize the nanoparticle $|W_p|$, divided by the total electromagnetic energy stored in the unperturbed resonator^{5,12} W_c ,

$$\frac{\Delta\omega}{\omega_0} = -\frac{\Delta\lambda}{\lambda_r} = -\frac{|W_p|}{W_c} \approx -\frac{\varepsilon_b \mathbf{E}_{p0}^{\dagger} \vec{\alpha}(\omega) \mathbf{E}_{p0}}{2 \int \varepsilon_0 \varepsilon_r |\mathbf{E}_0|^2 dV},\tag{1}$$

where ε_b is the permittivity of the background media, ε_0 is the permittivity of free space, ε_r is the dielectric constant of silica¹³, $\vec{\alpha}(\omega)$ is the polarizability tensor of the particle, \mathbf{E}_0 is the spatially-varying complex electric field amplitude for the WGM, \mathbf{E}_{p0} is the electric field amplitude for the unperturbed WGM at the location of the bound particle, and † represents the conjugate-transpose. The binding of a bioparticle will shift the resonance wavelength in the WGM resonator a miniscule amount. Another way to consider the cause of the resonance shift is that by entering the evanescent field of the WGM, the bound nanoparticle becomes part of the microcavity, which increases the effective round-trip path length. This increase in resonator path length causes the resonance wavelength to shift to longer wavelengths.

Label-free optical biosensors based on WGM cavities can detect macromolecules by tracking the resonance shift of the microcavity. The original method to track the resonance is by sweeping the wavelength of a tunable laser and measuring the transmission spectrum^{9,14}. However, this approach is limited by the wavelength scanning speed, which can be a few nanometers per second for piezo-tuned laser¹⁵. In the FLOWER system, Pound-Drever-Hall (PDH) locking technology¹⁶⁻¹⁸ is used to improve the response time of the biosensor, shortening the minimum detectable step interval to 1 ms. The PDH technology also improves the accuracy of tracking the WGM. WGM sensors have also been enhanced through coupling with plasmonic nanoparticles. The plasmon resonance provides a local enhancement of electric field in the numerator of Eq. (1), potentially leading to orders of magnitude resonance shift enhancement^{19,20}. The optical WGM resonators coupled with single gold nanorod can be utilized as a ultrasensitive

thermometer, which can resolve resonance shift that is smaller than 100 Hz²¹. Here we present the analytical basis for FLOWER, and construct a numerical simulation. Through the numerical simulation, we optimize the parameters of FLOWER and explore its limits of detection by analyzing the different noise effects.

II. METHODS

A. Overview of FLOWER

Figure 1 shows a schematic of the FLOWER system. An optical WGM microcavity is evanescently coupled to the system through a tapered optical fiber¹². A tunable continuous wave (CW) laser is locked to a WGM resonance using frequency locking. A frequency modulation dither signal is applied to the piezoelectric transducer in the tunable laser. Light is transmitted from the WGM resonator into an auto-balanced receiver, which can reduce laser intensity noise by $55 - 70 \text{ dB}^{22}$. The error signal, which is the time average of the product of the dither signal and receiver output signal, is proportional to the difference between the laser wavelength and the WGM resonance wavelength. A proportional-integral-derivative (PID) controller is used to control the laser wavelength. The PID controller receives the error signal and generates feedback to the laser controller to decrease the absolute value of the error signal to zero. In this way, the laser wavelength is locked at the WGM resonance wavelength. Therefore, we can measure shifts in WGM resonance in real time as particles bind by tracking the laser wavelength through the PID controller output. For these experiments, a tunable visible laser with wavelength approximately 633 nm is used due to the biophotonic diagnostic window where light absorption in water is minimal.

B. Numerical simulations

FLOWER's particle detection ability can be evaluated through numerical simulation. Mode-coupling theory and analytical modeling of the frequency locking process is used to generate a Simulink model. The limit of detection of FLOWER is affected by the spectral lineshape of the WGM resonance (e.g., Fig. 2a), which also determines the error signal used in the feedback loop when the resonance shifts (e.g., Fig. 2b). To derive the lineshape, the WGM resonator in Fig. 1(a) can be modeled using spatial coupled mode theory^{23,24}. When driven at a resonant wavelength $\lambda_0 = 2\pi c/\omega_0$, the real, time-dependent electric field can be written as,

$$E(r,t) = Re[G(t) \mathcal{E}(r) e^{j\omega_0 t}] = Re[A(t)\mathcal{E}(r)], \tag{2}$$

where G(t) is a slowly-varying amplitude function that accounts for injection or loss of light into the resonator at time scales long enough that a monochromatic approximation remains valid, $\mathcal{E}(\mathbf{r})$ describes the spatial variation of the complex electric field for the resonant mode, and $e^{j\omega_0 t}$ accounts for the high-frequency oscillations of the electric field wave. All time dependent terms are combined in A(t). In spatial coupled mode theory, the units of electric field are

partitioned between A and \mathcal{E} such that \mathcal{E} has unit power:

$$\int_{\mathcal{A}} \frac{1}{2Z} |\mathcal{E}(r)|^2 d^2 r = 1,\tag{3}$$

where \mathcal{A} is the cross-section of the mode field area, and Z is the characteristic impedance of the mode. Therefore, \mathcal{E} has units of V m⁻¹ W^{-1/2}, and A has units of W^{1/2}. The power of the travelling wave within the resonator is $|A(t)|^2$, and thus A is called power amplitude. We can correspondingly define an energy amplitude with units $J^{1/2}$,

$$a(t) = A(t) \sqrt{\frac{2\pi R}{v_g}},\tag{4}$$

where $2\pi R$ is the resonator circumference and v_g is the group velocity of the resonant mode. The energy stored within the resonator is $|a(t)|^2$.

The optical system in Fig. 1b is viewed as a lumped oscillator, which we assume an energy amplitude decay rate $1/\tau = 1/\tau_l + 1/\tau_e$, accounting for both intrinsic loss (l) and external power (e) coupling out from the resonator back into the fiber. The resonator is being driven by light coupled in from a tapered fiber carrying optical power $|s_i|^2$ with a real-valued mutual coupling coefficient μ between the resonator and fiber. The energy amplitude balance differential equation resulting from these assumptions is,

$$\frac{d}{dt}a = \left(j\omega_0 - \frac{1}{\tau}\right)a - j\mu s_i,\tag{5}$$

where the $j\omega_0$ term preserves the high-frequency time dependence in Eq. (2), and the -j coefficient in front of the μs_i term is an arbitrary phase factor for the incident light, which is commonly used in the literature²⁴. The relationship between μ and τ_e is $\mu^2 = 2/\tau_e$. The equation connecting the incident and transmitted amplitude down the output fiber is:

$$s_t = s_i - j\mu a,\tag{6}$$

where s_i represents the incident light amplitude and s_t represents the transmitted wave amplitude. Considering a steady state incident signal s_i with time dependency $s_i \sim \exp(j\omega t)$, which can be at a different frequency ω from the resonance frequency ω_0 , a solution to Eq. (5) is:

$$a = \frac{-j\sqrt{\frac{2}{\tau_e}}}{\frac{1}{\tau} + j(\omega - \omega_0)} s_i. \tag{7}$$

When this is introduced into Eq. (6), we have
$$\frac{s_t}{s_i} = 1 - \frac{\frac{2}{\tau_e}}{\frac{1}{\tau} + j(\omega - \omega_0)}.$$
 (8)

This equation describes the typical Lorentzian lineshape of a resonance, as plotted in Fig. 2a after taking the complex magnitude squared.

The quality factor of the resonator can be calculated by its definition as 2π times the ratio of the time averaged stored energy to the energy dissipated per optical circulation. We consider the case in which the microcavity is excited to an energy of $|a_0|^2$ and there is no incident light, $s_i = 0$. From Eq. (5), the microcavity energy decays as

$$|a(t)|^2 = |a_0|^2 \exp\left(\frac{-2t}{\tau}\right),$$
 (8)

The intrinsic loss of the microcavity is caused by scattering, absorption, and radiative process. For the resonator, the dissipated power caused by the intrinsic loss is

$$|s_l(t)|^2 = \frac{2}{\tau_l} |a(t)|^2.$$
 (9)

In the same case, from Eq. (6), the transmitted power is

$$|s_t(t)|^2 = \mu^2 |a(t)|^2 = \frac{2}{\tau_e} |a(t)|^2.$$
 (10)

The stored energy in microcavity is given by Eq. (8). The power coupled out of the resonator is given by Eq. (10), Thus

$$Q = \omega_0 \frac{|a(t)|^2}{|s_t(t)|^2 + |s_l(t)|^2} = \frac{\omega_0 \tau}{2},$$
(11)

where the stored energy is given by $|a|^2$ and the total dissipated power of the resonator is given by $|s_t|^2 + |s_l(t)|^2$. The Qfactor is inversely proportional to the loss of the WGM resonator. The high-O requirement of a biosensor can be routinely obtained experimentally in water with microtoroids³ or microspheres.⁵ The Q-factor can also be calculated from the transmission spectrum of the WGM resonator, shown in Fig. 2a. $Q = \frac{\Lambda_0}{\Lambda_\lambda}$, where $\Delta\lambda$ is the full width at half-maximum linewidth of the resonance. In Fig. 2a, the Q factor calculated from the transmission spectrum is equal to the Q factor calculated from Eq. (11).

In the FLOWER system, we modulate the frequency of the laser. The power amplitude of the laser output is:

$$A_{\rm las}(t) = A_0 e^{j[\omega_1 - \beta_0 \sin(\Omega t)]t}, \tag{12}$$

where β_0 is frequency modulation depth, and Ω is the dither signal frequency. The higher the frequency, the better the time resolution of the system. The frequency modulation bandwidth is limited by our choice of laser and Ω is set as $2\pi \times 2$ kHz. The incident light frequency is $\omega = \omega_1 - \beta_0 \sin(\Omega t)$, where ω_1 is the laser's central frequency without modulation. In the classical PDH technology, the laser is phase modulated by a Pockels cell¹⁷. In contrast, in our FLOWER system the tunable laser is frequency modulated by tuning the mirror position in the external cavity of the laser¹⁵. The 50:50 beam splitter splits the laser light into the signal and reference light. Neglecting losses in the beam splitter, laser coupling, and assuming a

perfectly adiabatic fiber taper, the incident light power in the vicinity of the microtoroid is half of the laser power $|s_i|^2 = |A_0|^2/2$, and the transmitted power is

$$|s_t|^2 = |s_i|^2 \left[1 - \frac{4}{\tau_l \tau_e} \times \frac{1}{\frac{1}{\tau^2} + (\omega - \omega_0)^2}\right].$$
 (13)

In the numerical simulation, Eq. (13) is used in the microcavity block for microcavity transmission. In the FLOWER system, the laser's central frequency ω_1 is extremely close to the microcavity resonance ω_0 . Through Taylor expansion about the point ω_0 , Eq. (13) becomes

$$|s_{t}|^{2} \approx \frac{|A_{0}|^{2}}{2} \left\{ 1 - \frac{4\tau^{2}}{\tau_{l}\tau_{e}} + \frac{4\tau^{4}}{\tau_{l}\tau_{e}} [\omega_{1} - \omega_{0} - \beta_{0}\sin(\Omega t)]^{2} \right\}.$$
(14)

The auto-balanced receiver converts the transmitted light power $|s_t|^2$ into electrical voltage

$$v_{PD} = (r_{PD} + r_{ext}) \cdot R \cdot |s_t|^2, \tag{15}$$

where r_{PD} is the internal resistance of auto-balanced receiver, r_{ext} is the additional external resistance for the receiver and R is the responsivity of the photodiode in the receiver in A W⁻¹. The auto-balanced receiver circuitry can automatically adjust the gain g to satisfy the balance equation $|s_t|^2 - g \cdot |s_r|^2 = 0$ at direct current (DC). As such, the auto-balanced receiver removes the DC component of the receiver output voltage v_{PD} . Then the auto-balanced receiver output voltage becomes:

$$v_{receiver} = \frac{|A_0|^2 (r_{PD} + r_{ext})R}{2} \cdot \frac{4\tau^4}{\tau_l \tau_e} \times \left[-2(\omega_1 - \omega_0)\beta_0 \sin(\Omega t) - \frac{\beta_0^2}{2} \cos(2\Omega t) \right], \tag{16}$$

In the numerical simulation, the receiver block consists of Eq. (16) and the balance equation. The receiver output voltage is mixed with the dither signal, $\sin(\Omega t)$. Time averaging the mixed signal generates the error signal v_{error} :

$$v_{error} = \frac{\Omega}{2\pi} \times \int_0^{\frac{2\pi}{\Omega}} v_{receiver} \cdot \sin(\Omega t) dt$$

= $-|A_0|^2 (r_{PD} + r_{ext}) R \cdot \frac{2\tau^4}{\tau_1 \tau_e} \cdot \beta_0(\omega_1 - \omega_0).$ (17)

This equation represents the central, linear part of the error signal plotted in Fig. 2b, where the linearization used in the Taylor expansion in Eq. (14) is valid. The coefficients in front of $(\omega_1 - \omega_0)$ are constant and show that the error signal is proportional to the difference between the laser frequency and the WGM resonance. Inputting the error signal to the PID controller provides a feedback loop to the laser, which can stabilize the laser's frequency and lock the laser's central

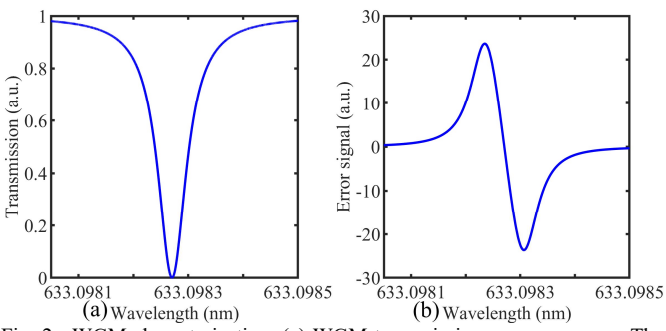


Fig. 2. WGM characterization. (a) WGM transmission near resonance. The Q-factor of the WGM resonator is 10^7 . (b) The error signal v_{error} is generated by demodulating the 2kHz dither signal from the receiver output. The frequency modulation amplitude is 60 MHz.

wavelength ω_1 to the resonance of the microcavity ω_0 . Eq.(17) is used in the average block in the Simulink model.

C. Simulink

Using Simulink, we built a simulation system based on the schematic of FLOWER shown in Fig. 1a. The full Simulink model is shown in the Appendix A. The input laser power is set at 2 mW. Initially, the laser output wavelength is 633 nm plus the dither signal. The microtoroid in Fig.1b is simulated using the optical resonator transmission Eq. (13). The receiver is simulated in Simulink using Eq. (15). Fig. 2a shows an ultrahigh Q microcavity resonance (Q = 1.01×10^7) at 633.09826 nm wavelength. In Fig. 2b, the error signal is acquired by scanning the laser wavelength. This curve shows that the error signal is proportional to the difference between the tunable laser wavelength and microtoroid resonance in the range 633.09825 nm - 633.09827 nm. Therefore, the FLOWER system can remain locked to the microcavity resonance only when the discrete shifts in resonance wavelength are smaller than 10 fm. During frequency locking, the microcavity resonance wavelength can be calculated from the PID output voltage.

III. RESULTS AND DISCUSSION

The closed loop system total noise level and response time determine the detectable particle size and time resolution of the system. In the simulation, we optimize the system parameters for the minimum detectable particle size and resolvable step interval.

A. Noise level determination

The FLOWER system has three main noise sources: (1) shot noise from the photodiode in the auto-balanced receiver, (2) laser intensity noise, which is defined as fluctuations in the output power of the laser, and (3) laser phase noise, which leads to a finite laser linewidth.

Shot noise from the photodiode in the auto-balanced receiver (Nirvana™ Auto-Balanced Optical Receivers 2007²⁵)

The auto-balanced receiver is limited by shot noise. The mean power of the shot noise for a single photodiode in the auto-balanced receiver is²⁶:

$$\sigma_{shot}^2 = 2eRP_{signal}\Delta f, \tag{18}$$

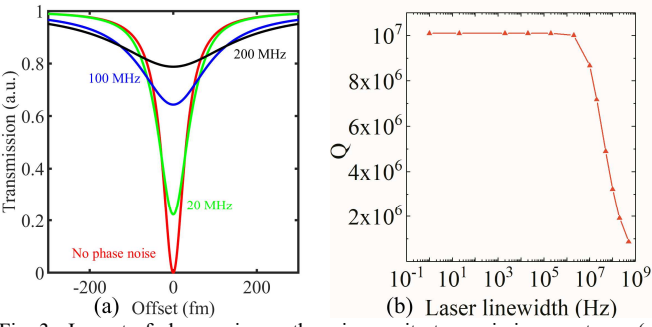


Fig. 3. Impact of phase noise on the microcavity transmission spectrum. (a) Phase noise broadens and reduces the contrast of the resonance dip due to broadening of the laser linewidth. The red curve neglects phase noise. The laser linewidths for the other curves are shown in the plot. (b) The observed extrinsic O factor of the microcavity as a function of laser linewidth.

where e is the electron charge, P_{signal} is the power of the incident light and Δf is the 3 dB bandwidth of the photodiode, which is 125 kHz²⁵. The SNR of the shot noise is the ratio of the mean power of the electrical signal P_e over the mean power of the shot noise σ_{shot}^2 :

$$SNR_{shot\ noise} = \frac{\langle P_e \rangle}{\sigma_{shot}^2} = \frac{(R|s_t|^2)^2}{2eR|s_t|^2 \Delta f} = \frac{R|s_t|^2}{2e\Delta f}$$

$$= 121 \text{ dB}. \tag{19}$$

Increasing the incident optical power can improve the SNR of the shot noise. However, the incident optical power is limited by the saturation power of the auto-balanced receiver. In the numerical simulation, the signal and reference power of the auto-balanced receiver are set close to the receiver's saturation power (1 mW). As a result, the SNR of the shot noise is 121 dB in the numerical simulation.

Laser intensity noise

The relative intensity noise (RIN) of the tunable laser (Velocity TLB-6704) is -117 dB/Hz¹⁵. The SNR of the laser intensity noise measured by the receiver is the ratio of the receiver electrical signal power $\langle P_e \rangle$ over the receiver electrical noise power δP_e caused by the laser intensity noise, excluding any contributions from shot noise and thermal noise²⁷⁻²⁹

$$SNR_{intensity\ noise} = \frac{\langle P_e \rangle}{\delta P_e} = \frac{\langle i_s^2 \rangle}{\langle i_n^2 \rangle} = \frac{\langle |s|^4 \rangle}{\langle (\Delta |s|^2)^2 \rangle}$$

$$= \frac{1}{RIN \times \Delta f}$$

$$= \frac{1}{10^{-11.7} \text{Hz}^{-1} \times 125000 \text{ Hz}} = 4.0095 \times 10^6,$$
(20)

where i_s is the receiver electrical signal current and i_n is the receiver electrical current noise. The SNR of the intensity noise can be expressed in the logarithmic decibel scale $SNR_{intensity\ noise} = 66.03dB$. Additionally, the auto-balanced receiver can suppress the laser intensity noise by $55-70\ dB^{22}$. Therefore, the SNR of the intensity in the FLOWER system is 121.03-136.03dB, which is approximately the same level as

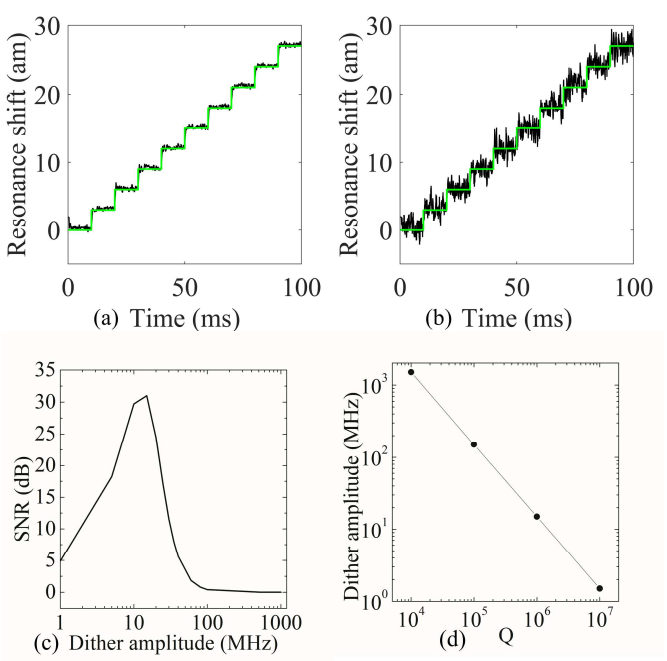


Fig. 4. Individual particles bind to the microcavity at a time interval of 10 ms. The dither amplitude affects the SNR of the resonance wavelength shift caused by particle binding. The green curves in (a) and (b) show the true the real particle binding events. (a) The Q of this microcavity is 10^6 and the dither frequency amplitude is 15 MHz (20 fm in wavelength). The step height is set at 3 am. (b) The dither amplitude is changed to 100 MHz (134 fm in wavelength) and the step height is 3 am. The difference in noise level is apparent. (c) The SNR of the resonance wavelength shift response for different dither frequency amplitudes. The optimal dither amplitude is 15 MHz for this resonance. (d) Higher quality factor WGMs result in smaller optimal dither amplitude.

shot noise in the auto-balanced receiver.

Laser phase noise

The origin of the laser phase noise is the quantum noise from spontaneous emission into the cavity mode³⁰ and some technical noise, (e.g. vibration of cavity mirrors or temperature fluctuations). The phase noise leads to a finite linewidth of the tunable laser. In the numerical simulation, the laser power spectrum is considered as a normalized Lorentzian shape³¹. Considering the phase noise, the power amplitude of the tunable laser is changed to:

$$A_{\text{las}}(\omega, t) = A_0 \sqrt{\frac{1}{\pi} \frac{\frac{1}{2}\Gamma}{(\omega - \omega_1)^2 + (\frac{1}{2}\Gamma)^2}} e^{j[\omega_1 - \beta_0 \sin(\Omega t)]t}, \quad (21)$$

where ω is the laser optical frequency, and Γ is the laser linewidth. The microcavity transmitted power becomes:

$$|s_{t}|^{2} = \int_{-\infty}^{+\infty} \frac{1}{2} |A_{\text{las}}(\omega, t)|^{2} \times \left[1 - \frac{4}{\tau_{l} \tau_{e}} \times \frac{1}{\frac{1}{\tau^{2}} + (\omega - \omega_{0})^{2}}\right] d\omega$$
 (22)

In the numerical simulation, Eq.(22) describes the transmission in the microcavity block when phase noise is considered.

In Fig. 3a, compared to the resonance without phase noise (red curve), whose minimum value is 0, the minimum value of the resonance for a 20 MHz linewidth phase-noise-broadened laser (green curve) is increased to 0.2226. When the finite linewidth laser is scanned to the resonance wavelength, the tails of the laser spectrum are detuned from the resonance wavelength of the WGM. The transmitted power for this part of the laser spectrum is greater than zero, reducing the depth of the transmission dip.

The intrinsic Q factor of the microcavity is 1.01×10^7 , which is calculated from Eq. (11). In Fig. 3b, when the laser linewidth is greater than 2 MHz, it broadens the microcavity transmission spectrum, and the extrinsic Q factor of the resonance begins to drop significantly. However, when the laser linewidth is smaller than 2 MHz, the Q value remains approximately at its intrinsic value and phase noise has a negligible impact on the transmission spectra, and hence a negligible impact on the response function we use to model the microcavity in Simulink. In the FLOWER system, the linewidth of the tunable laser is 200 kHz, which is significantly smaller than 2 MHz, and therefore, we neglect phase noise in the remainder of our results presented below.

B. Effect of dither amplitude

Figure 4 shows the relationship between the system SNR and the dither amplitude. In Fig. 4a, the resonance shift curve records every step caused by particle binding. In Fig 4b, the steps input into the Simulink model are the same as in Fig. 4a, but the dither amplitude is increased from 15 MHz to 100 MHz, resulting in a greatly reduced SNR. The accuracy for the measured step positions and heights are correspondingly reduced. For a microcavity with $Q = 10^6$, the SNR in response to 3 am input steps reaches a maximum value of 30.9 dB when the frequency modulation depth $\beta_0 = 2\pi \times 15 \text{ MHz}$. The relationship between the optimal dither amplitude and microcavity Q-factor is shown in Fig. 4d. A larger error signal slope can provide a larger gain for the feedback loop for a given difference between laser wavelength and microcavity resonance. For the optimal frequency modulation depth, it is best to maximize the error signal slope. We find that the ratio of optimal dither wavelength amplitude over the resonance linewidth is a constant

$$\frac{\lambda_{dither}}{\Delta \lambda} = \frac{\beta_0}{\omega_0} Q = 0.03196. \tag{23}$$

The classical PDH technology uses a phase modulation with phase modulation depth β_p . The experiment setup usually restricts the Q factor of the cavity and the laser wavelength choice. For the classical PDH technology, people often adjust the phase modulation depth β_p for high sensitivity. The optimal modulation depth β_p is 1.08 for the restricted Q factor of cavity and laser wavelgnth³². Instead, the FLOWER introduces a direct frequency modulation into the tunable laser output. The optimal frequency modulation β_0 depends on the laser frequency and the cavity's Q factor through the Eq.(23).

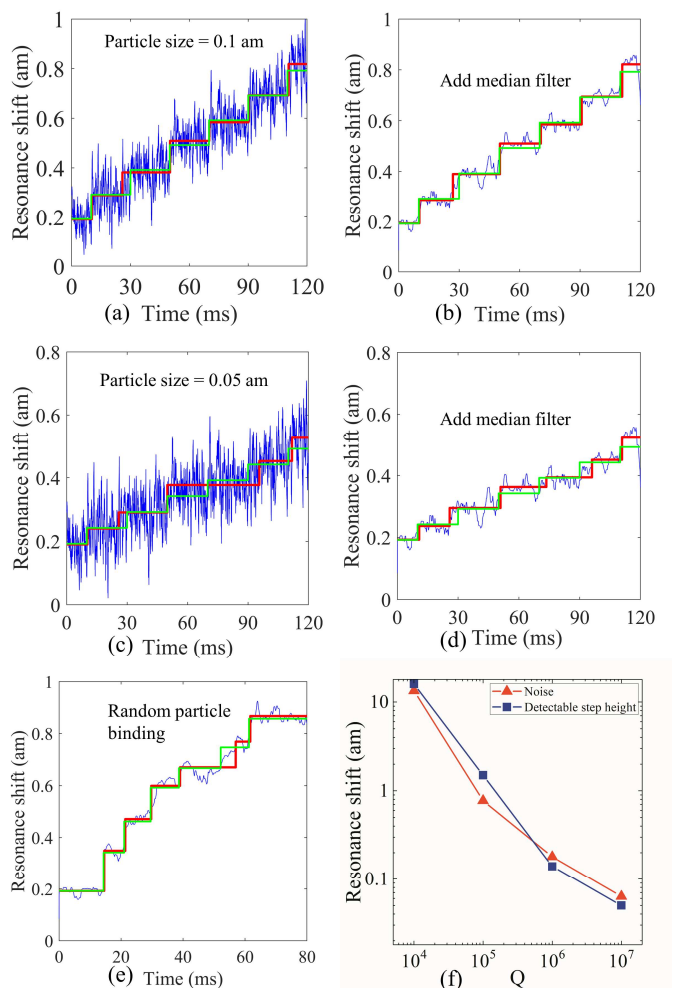


Fig. 5. Limit of detection in small particle sensing. (a)-(e) Step traces in response to simulated particle binding events. Green curves are the true binding events input into our model. Blue curves represent raw output data (a), (c) or data processed using a median filter with a 3 ms window (b), (d), (e). Red curves are the result of an automated step-finding algorithm operating on the blue curve. Step heights are either 0.1 am (a), (b), 0.05 am (c), (d), or randomly drawn e. Step time intervals are either 20 ms (a)-(d) or randomly drawn (e). (f) Comparison between empirically determined limit of detection and output noise level for different microcavity quality factors when using an optimal dither amplitude. The noise level is based on the raw trace data, and the detectable step height is based on the on the trace after median filtering and step-fitting algorithm.

C. Effect of data post-processing

The use of step-finding algorithms and a median filter can enable better single particle resolution 33,34 . Figure 5 shows the simulation results from a microcavity with $Q=10^7$. A step-fitting algorithm 34 is used to find all the steps based on either the raw data or filtered data. In Fig. 5b, the median filter removes most of the high-frequency oscillations in the raw data. The step-fitting algorithm can find the step height and position precisely. For these 0.1 am steps, the error between the recovered step heights and those input into the simulation is less than 10%. When the step height is reduced to 0.05 am (Fig. 5c), the step-fitting algorithm finds five steps in the raw data; one step at time t=70 ms is missed. However, after median filtering with a 3 ms window, all six steps are recovered (Fig. 5d).

In a real experiment, the time interval between particle

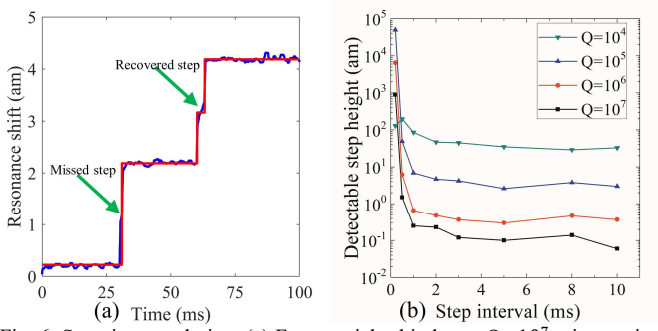


Fig. 6. Step time resolution. (a) Four particles bind on a $Q\sim10^7$ microcavity. In this case, an individual particle causes a 1 am resonance shift. The blue curve is the resonance shift after a 3 ms median filter has been applied. The red curve is a step-fit graph based on the blue curve. (b) Step parameters necessary for accurate detection. Binding events above a curve (larger heights and/or longer time intervals) can be accurately recovered by a WGM of the corresponding Q.

binding events is random. Fig. 5e shows 6 particles binding to a microcavity at random time intervals drawn from a Poisson distribution with expected value 15 ms. The particle size (defined here by the step height of the expected resonance shift) varies from 0.07 am to 0.16 am. In Fig. 5e, the step-fitting curve precisely captures the particle binding events, and the recovered step heights match the input particle sizes. Fig. 5f demonstrates the relationship between noise level of the resonance shift data and minimum resolvable step height. Their values both decrease as the Q-factor of the microcavity increases. The minimum resolvable step height is approximately equal to the noise of the FLOWER system.

D. Time resolution

The time resolution of the system is also important, especially for measuring discrete binding events in analyte solutions of high concentration. The minimum resolvable time interval between steps depends on the step height and Q-factor (Fig. 6). Our simulations indicate this to be only slightly longer than the system response time, which is based on the dither frequency period of 0.5 ms. The median filter window also affects the time resolution. After trying different median filter windows, 3 ms is the optimal median filter window for particle binding event detection.

In Fig. 6a, four particles in total bind on a microcavity over 100 ms. The binding of two particles happens around 30 ms. The time between these two particle binding events is 1 ms. Using the step-fitting algorithm, the system is unable to distinguish the two separate steps and fits them as a single step of double height. The other two particles bind at around t=60 ms. The time between these two binding events is 3 ms. In this case, the two separate steps are clearly distinguished after stepfitting. Fig. 6b demonstrates the relationship between the minimum distinguishable step time interval and the minimum detectable step height after median filtering and step-fitting. If the error between the recovered step time and input step time is less than 1 ms and the error in recovered step height is less than 35%, we consider the step to be accurately recovered. The minimum recoverable step height is relatively constant for time intervals longer than 1 ms, but diverges rapidly for intervals shorter than 1 ms. We therefore conclude that the response time of the simulated FLOWER system is 1 ms. This response time

is mainly determined by the dither signal frequency (here 2 kHz) and the PID controller response. In the simulation, the appropriate P, I, D parameters (P=0.1, I=800, D=300) are applied to the PID controller. This makes the minimum detectable step interval of the system close to the dither period. The fast response time reduces the impact of low frequency noise, such as 1/f noise, mechanical vibration, and thermal noise. In Fig. 6a, the step height error is the noise accumulation over the step rise time. For low frequency noise, the accumulated error is quite small compared to the step height. Therefore, low frequency noise sources are ignored in the numerical simulation.

IV. CONCLUSION

In conclusion, our work examines through numerical simulation the limits of detection of FLOWER in response to discrete particle binding events. The shot noise from the receiver and the laser intensity noise both affect the limit of detection for small particle binding events. The SNR of the system can be optimized through a choice of dither frequency amplitude, use of higher quality factor microcavities, and by increasing the laser power of the system along with a photodetector capable of handling that power. Based on these results, using existing commercial equipment, FLOWER is expected to be capable of detecting 0.05 attometer shifts at time intervals under one millisecond. The optimal dither amplitude was found to be 0.032 times the resonance linewidth. Higher quality factor micro-resonators can reduce the noise level and lower the minimum resolvable step height. For a fixed Q value microcavity, acousto-optic modulation can substitute direct frequency modulation of the laser. The bandwidth of an acousto-optic modulator can be as high as 27 MHz³⁵. For a wide range of modulation frequencies, we can adjust the gain parameter in the PID controller for tight and stable frequency locking. Use of a broad bandwidth acousto-optic modulator in FLOWER or a lithium niobite phase modulator could greatly increase the dither signal frequency. This can also decrease the response time of the total system and improve the detectable step time resolution.

APPENDIX A

A. Details of the numerical simulation of FLOWER in Simulink

To achieve frequency locking, the initial laser wavelength should approach the microcavity resonance. The initial laser wavelength is in units of nanometers. This constant value is added to the PID output signal to set the laser wavelength. This dynamic wavelength is what FLOWER tracks as particles bind. The dither signal output voltage is converted to a wavelength signal. The converter output signal is added to the laser wavelength to simulate frequency modulation. The power component sets the laser power to 2 mW. Additive Gaussian white noise (AGWN) is added to the laser intensity. The power signal and the frequency signal pass through the microcavity to yield the transmitted power in mW. The transmitted power through microcavity can be calculated using Eq. (14) in the main text. In the microcavity block, the input parameter P is the incident light power $P = |s_i|^2 = |A_0|^2/2$, the w represents the

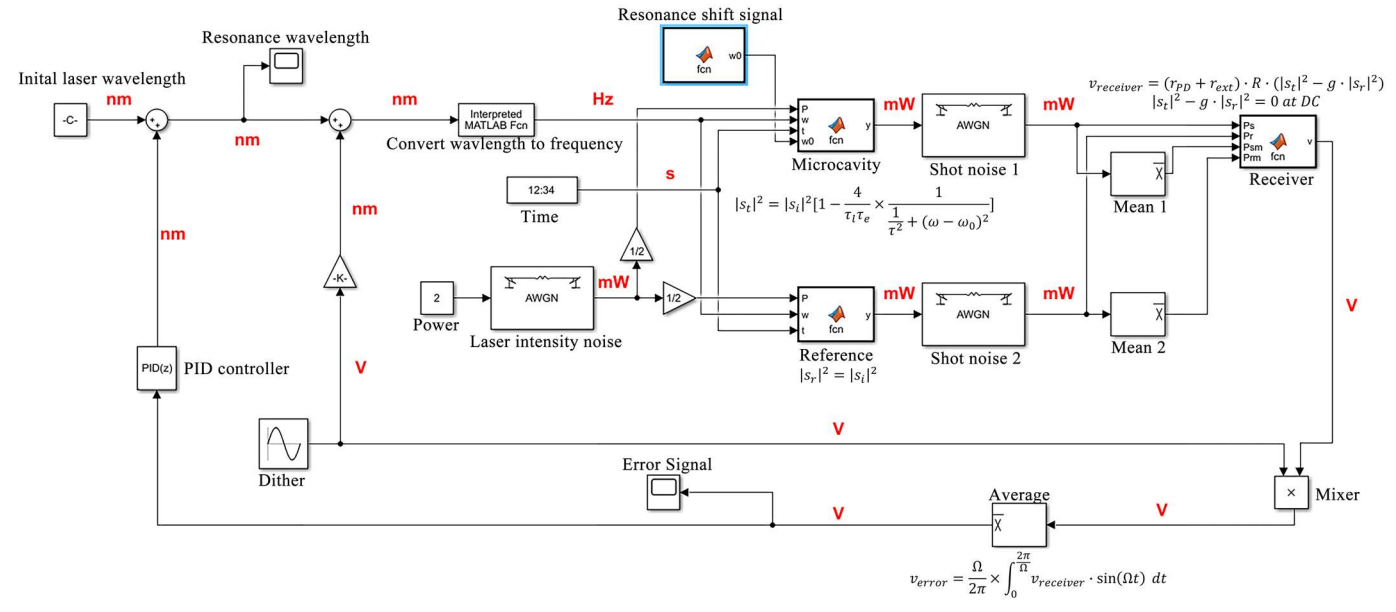


Fig. 7. FLOWER Simulink model

incident light angular frequency ω , and the w0 stands for the microcavity resonance angular frequency ω_0 . The resonance shift signal block sends a signal to change the resonance frequency ω_0 of the microcavity. The reference signal equals half of the tunable laser power $|s_r|^2 = |s_i|^2 = |A_0|^2/2$. In the reference block, the input P represents the reference light power $P = |s_r|^2$ and w stands for the reference light angular frequency ω .

The transmitted power and reference power are separately added with shot noise by the shot noise AGWN components. Although shot noise a Poisson process, it can be approximated here as AGWN. For small photon counts, the shot noise is low, and the system is dominated by other noise sources, making the error between Gaussian and Poisson distributions insignificant. For large photon counts, the central limit theorem ensures that the Poisson distribution approaches a Gaussian distribution. Therefore, the shot noise is approximately modeled using a Gaussian distribution.

The Mean 1, 2 and Receiver parts work as the auto-balanced receiver, which converts the input power to an output voltage signal in volts. For the receiver, the output voltage is calculated from Eq. (16) in the paper. The auto-balanced receiver output voltage is $v_{receiver} = (r_{PD} + r_{ext}) \cdot R \cdot (|s_t|^2 - g \cdot |s_r|^2)$. The adjusted reference channel gain g equals to the ratio of signal to reference power, which can automatically adjust to ensure the balance equation $|s_t|^2 - g \cdot |s_r|^2 = 0$. The auto-balancing is the result of a low frequency f_{cutoff} feedback loop that adjusts the reference channel gain g. The gain-compensation cutoff frequency f_{cutoff} must be set below 2 kHz, which corresponds to the dither frequency. So that noise cancellation is not degraded. In the receiver block, the input parameter Ps represents the light power from signal channel, Pr is for the reference channel light power, Psm stands for the DC component (time average) of Ps, and Prm stands for the DC component of Pr. The receiver output signal is mixed with the dither voltage to generate a voltage signal. The voltage signal is transformed into an error signal through the averaging

components. The averaging process is described by Eq. (18) in main text. The error signal is in units of volts. The PID controller uses the error signal to generate a wavelength signal, which moves the laser's wavelength. After the PID block, the converter block converts the PID output voltage signal to wavelength signal using the ratio is 2×10^{-5} nm/ $_{V}$. This parameter is adjusted based on the frequency locking condition in the system by observing the resonance shift signal. If the resonance shift signal has a large oscillation, the parameter P should be decreased until the resonance shift signal stabilizes to a constant value. If the resonance shift trace has a small oscillation near the step, then the parameter I should increase, and P should decrease to keep $P \cdot I$ constant until the fluctuation of the resonance shift signal disappears. The appropriate P, I, D parameters (P = 0.1, I = 800, D = 300) are chosen based on the error signal. When suitable PID parameters are applied to FLOWER, the error signal can rapidly drop to zero. We note that for this simulation, the time input into the microcavity is unnecessary but for other microresonator applications such as beat signal detection, the phase of the electric field is necessary, and the time block is needed.

B. Step-fitting algorithm

Finding steps

The step-fitting algorithm³⁴ adds a large step first. The first large step is positioned is to minimize the χ^2 value of the fit. The left plateau value equals the average of the data on the left side of the first step. The right plateau value equals the average of the data on the right side of the first step. The step size is the difference between the left plateau value and the right plateau value. Subsequent steps are found by adding new steps to the plateaus of the previous steps. Each time, one new step is added to the previous plateaus. Each new step is positioned to minimize the χ^2 value.

Evaluating step fits

The number of fitting steps is essential. If the fitting step number is small, the step fit is underfit and there are still some steps hidden in the data. If the data is fit with more steps than

the real step number, the step fit is overfit. Some small fake steps are divided by the real large steps. For the best step fit, the number of the fitting steps is equal to the number of the real steps in data. To find the best step fit, a counter-step fit is generated based on the step fit. Every counter-step is found on the plateau of the corresponding step fit by minimizing the χ^2 value of the counter-step fit. In this way, each counter-step fit has the same step number with the corresponding step fit. A 'step indicator' S is defined as the ratio between the χ^2 value of the step fit and the χ^2 value of counter-step fit. The step indicator S continually increases until the step fit is the best step fit; then the ratio S decreases slowly to \sim 1. The best step fit corresponds to the maximum of the step indicator S.

REFERENCES

- [1] Su, J. Portable and sensitive air pollution monitoring. *Light Sci. Appl.* 7, (2018).
- [2] He, L., Özdemir, Ş. K., Zhu, J., Kim, W. & Yang, L. Detecting single viruses and nanoparticles using whispering gallery microlasers. *Nat. Nanotechnol.* 6, 428–432 (2011).
- [3] Su, J. Label-Free Single Exosome Detection Using Frequency-Locked Microtoroid Optical Resonators. ACS Photonics 2, 1241–1245 (2015).
- [4] Fan, X. et al. Sensitive optical biosensors for unlabeled targets: A review. Anal. Chim. Acta 620, 8–26 (2008).
- [5] Amold, S., Khoshsima, M., Teraoka, I., Holler, S. & Vollmer, F. Shift of whispering-gallery modes in microspheres by protein adsorption. Opt. Lett. 28, 272 (2003).
- [6] Armani, D. K., Kippenberg, T. J., Spillane, S. M. & Vahala, K. J. Ultra-high-Q toroid microcavity on a chip. Nature 421, 925–928 (2003).
- [7] Su, J., Goldberg, A. F. & Stoltz, B. M. Label-free detection of single nanoparticles and biological molecules using microtoroid optical resonators. Light Sci. Appl. 5, e16001 (2016).
- [8] Vahala, K. J. Optical microcavities. Nature 424, 839 (2003).
- [9] Vollmer, F., Arnold, S. & Keng, D. Single virus detection from the reactive shift of a whispering-gallery mode. Proc. Natl. Acad. Sci. 105, 20701–20704 (2008).
- [10] Baaske, M. D., Foreman, M. R. & Vollmer, F. Single-molecule nucleic acid interactions monitored on a label-free microcavity biosensor platform. Nat. Nanotechnol. 9, 933–939 (2014).
- [11] Ghali, H., Chibli, H., Nadeau, J. L., Bianucci, P. & Peter, Y.-A. Real-Time Detection of Staphylococcus Aureus Using Whispering Gallery Mode Optical Microdisks. Biosensors 6, 20 (2016).
- [12] Waldron, R. A. Perturbation theory of resonant cavities. Proc. IEE -Part C Monogr. 107, 272–274 (1960).
- [13] Novotny, L. & Hecht, B. Principles of Nano-Optics. (Cambridge University Press, 2012).
- [14] Carmon, T., Yang, L. & Vahala, K. J. Dynamical thermal behavior and thermal self-stability of microcavities. Opt. Express 12, 4742–4750 (2004).
- [15] TLB-6704. https://www.newport.com/p/TLB-6704.
- [16] Carmon, T. et al. Feedback control of ultra-high-Q microcavities: application to micro-Raman lasers and micro-parametric oscillators. Opt. Express 13, 3558–3566 (2005).
- [17] Black, E. D. An introduction to Pound–Drever–Hall laser frequency stabilization. Am. J. Phys. 69, 79–87 (2000).
- [18] Weng, W., Anstie, J. D. & Luiten, A. N. Refractometry with Ultralow Detection Limit Using Anisotropic Whispering-Gallery-Mode Resonators. Phys. Rev. Appl. 3, 044015 (2015).
- [19] Swaim, J. D., Knittel, J. & Bowen, W. P. Detection limits in whispering gallery biosensors with plasmonic enhancement. Appl. Phys. Lett. 99, 243109 (2011).
- [20] Shopova, S. I., Rajmangal, R., Holler, S. & Arnold, S. Plasmonic enhancement of a whispering-gallery-mode biosensor for single nanoparticle detection. Appl. Phys. Lett. 98, 243104 (2011).
- [21] Heylman, K. D. et al. Optical microresonators as single-particle absorption spectrometers. Nat. Photonics 10, 788–795 (2016).
- [22] Hobbs, P. C. D. Ultrasensitive laser measurements without tears. Appl. Opt. 36, 903 (1997).

- [23] Fan, S., Suh, W. & Joannopoulos, J. D. Temporal coupled-mode theory for the Fano resonance in optical resonators. JOSA A 20, 569– 572 (2003).
- [24] Little, B. E., Chu, S. T., Haus, H. A., Foresi, J. & Laine, J.-P. Microring resonator channel dropping filters. J. Light. Technol. 15, 998–1005 (1997).
- [25] 2007. https://www.newport.com/p/2007.
- [26] Deen, M. J. & Kumar, S. Fiber Optic Communications. 573.
- [27] Levi, A. Essential Semiconductor Laser Device Physics. (IOP Publishing, 2018). doi:10.1088/978-1-6432-7028-9.
- [28] Intensity modulation and noise characterization of high-speed semiconductor lasers - IEEE Journals & Magazine. https://ieeexplore.ieee.org/abstract/document/93288.
- [29] Coldren, L. A., Corzine, S. W. & Mashanovitch, M. Diode lasers and photonic integrated circuits. (Wiley, 2012).
- [30] Gardiner, C., Zoller, P. & Zoller, P. Quantum Noise: A Handbook of Markovian and Non-Markovian Quantum Stochastic Methods with Applications to Quantum Optics. (Springer Science & Business Media, 2004).
- [31] Hinkley, E. D. & Freed, C. Direct Observation of the Lorentzian Line Shape as Limited by Quantum Phase Noise in a Laser above Threshold. Phys. Rev. Lett. 23, 277–280 (1969).
- [32] Black, E. D. An introduction to Pound–Drever–Hall laser frequency stabilization. Am. J. Phys. 69, 79–87 (2000).
- [33] Carter, B. C., Vershinin, M. & Gross, S. P. A Comparison of Step-Detection Methods: How Well Can You Do? Biophys. J. 94, 306–319 (2008).
- [34] Kerssemakers, J. W. J. et al. Assembly dynamics of microtubules at molecular resolution. Nature 442, 709–712 (2006).
- [35] Kotov, V. M. Broadband Acousto-Optic Modulation of Optical Radiation. Acoust. Phys. 65, 369–373 (2019).



Shuang Hao received a B.S. in optical sciences from Huazhong University of Science and Technology, Wuhan, Hubei, China in 2015. He is currently pursuing a Ph.D. in Optical Sciences at the University of Arizona, Tucson, AZ, USA.

From 2014 to 2015, he was a Research Assistant with the Nanophotonics Lab,

National Laboratory for Optoelectronics, Wuhan, Hubei, China. His research interests include nanoscale photonic technologies for biosensing and optical comb generation using ultra-high Q microcavities.



Judith Su was born in College Station, TX, USA, and received a B.S. and M.S. degree in mechanical engineering from MIT, Cambridge, MA, USA in 2002 and 2004, respectively and a PhD in Biochemistry & Molecular Biophysics from Caltech, Pasadena, CA, USA in 2014

Since 2017, she has been an Assistant Professor in the Wyant College of Optical

Sciences and Department of Biomedical Engineering at the University of Arizona, Tucson, AZ, USA. She is also a Visiting Associate at Caltech, on the Editorial Advisory Board of Translational Biophotonics, a member of the Scientific Advisory Board of Femtorays Technologies, and on the Board of Scientific Counselors for the National Institute for Occupational Safety and Health (NIOSH) and Safety. Her research interests are in imaging, microfabrication, and optical

instrument building for biological and medical applications. She holds 5 patents on microcavity sensors.